

---

# ON THE PREDICTIVE SKILL OF ARTIFICIAL INTELLIGENCE-BASED WEATHER MODELS FOR EXTREME EVENTS USING UNCERTAINTY QUANTIFICATION

---

A PREPRINT

**Rodrigo Almeida**

Applied Machine Learning Group  
Fraunhofer Heinrich-Hertz Institute  
10587 Berlin, Germany  
rodrigo.almeida@hhi.fraunhofer.de

**Noelia Otero**

Applied Machine Learning Group  
Fraunhofer Heinrich-Hertz Institute  
10587 Berlin, Germany

**Miguel-Ángel Fernández-Torres**

Signal Theory and Communications Dept.  
Universidad Carlos III de Madrid (UC3M)  
28911 Leganés, Madrid, Spain

**Jackie Ma**

Applied Machine Learning Group  
Fraunhofer Heinrich-Hertz Institute  
10587 Berlin, Germany

November 24, 2025

## Abstract

Accurate prediction of extreme weather events remains a major challenge for artificial intelligence-based weather prediction systems. While deterministic models such as FuXi, GraphCast, and SFNO have achieved competitive forecast skill relative to numerical weather prediction, their ability to represent uncertainty and capture extremes is still limited. This study investigates how state-of-the-art deterministic artificial intelligence-based models respond to initial-condition perturbations and evaluates the resulting ensembles in forecasting extremes. Using three perturbation strategies (Gaussian noise, Hemispheric-Centered Bred Vectors, and Huge Ensembles), we generate 50-member ensembles for two major events in August 2022: the Pakistan floods and the China heatwave. Ensemble skill is assessed against ERA5 and compared with IFS ENS and the probabilistic AIFSENS model using deterministic and probabilistic metrics. Results show that flow-dependent perturbations produce the most realistic ensemble spread and highest probabilistic skill, narrowing but not closing the performance gap with numerical weather prediction ensembles. Across variables, artificial intelligence-based weather models capture temperature extremes more effectively than precipitation. These findings demonstrate that input perturbations can extend deterministic models toward probabilistic forecasting, paving the way for approaches that combine flow-dependent perturbations with generative or latent-space uncertainty modeling for reliable artificial intelligence-driven early warning systems.

## 1 Introduction

Artificial Intelligence (AI) is rapidly reshaping the field of weather and climate forecasting, including the assessment and management of natural hazard risks [Camps-Valls et al., 2025]. Traditionally, Numerical Weather Prediction (NWP) relies on solving complex systems of partial differential equations to simulate atmospheric processes. However, this approach demands substantial computational resources, which constrains both spatial and temporal resolution. Given the inherently chaotic nature of the atmosphere, it is also crucial to account for uncertainties in both the initial conditions and the model itself. Ensemble forecasting addresses

this challenge by generating multiple simulations to represent a range of possible outcomes, forming the basis for probabilistic forecasts [Leutbecher and Palmer, 2008].

With recent advances in machine learning (ML), the development of sophisticated deep learning (DL) models, and the increasing availability of large datasets, data-driven AI approaches are gaining traction—offering promising improvements to traditional forecasting methods. AI-based weather prediction (AIWP) models using transformers [Bi et al., 2023, Chen et al., 2023a,b, Allen et al., 2025], Fourier neural operators [Bonev et al., 2023, Kurth et al., 2023], and graph neural networks [Keisler, 2022, Lam et al., 2023] have pushed the skill of weather forecasting over what is considered state of the art for NWP models. Moreover, the recent operational integration of the AI Forecasting System (AIFS), developed by the European Centre for Medium-Range Weather Forecasts (ECMWF), alongside traditional NWP models, marks a significant milestone in the evolution of AIWP [Lang et al., 2024a].

Generative approaches have also been introduced, making use of diffusion-based models such as GenCast [Price et al., 2024], which have the ability to directly produce a distribution of potential future weather states. Similarly, Li et al. [2024] presented SEEDS, a Scalable Ensemble Envelope Diffusion Sampler to generate an arbitrarily large ensemble conditioned on as few as one or two forecasts from an operational NWP system. Furthermore, hybrid approaches like NeuralGCM [Kochkov et al., 2024] combine the dynamical core of traditional NWP models with local ML-based parameterizations, achieving performances comparable to operational ensemble forecasts.

Deterministic AIWP models have been found to underperform NWP in forecasting extreme events, since they are usually trained with a deterministic objective, which rewards the reduction of the variance of the predictions [Brenowitz et al., 2024]. At the same time, these models have been found to capture and appropriately simulate physical laws in the atmosphere [Baño-Medina et al., 2025a]. Olivetti and Messori [2024] reported that, although deterministic AIWP models outperform deterministic NWP for extreme events, they show differing skill depending on the region and extreme event. Specifically, they tend to perform best for temperature, at short lead times, and near the tropics. Zhang et al. [2025] and Zhao et al. [2025] report similar findings, specifically for warm extremes and wet extremes.

While most of these models are currently outperforming deterministic NWP [Rasp et al., 2024], providing probabilistic forecasts, as in IFS-ENS [Molteni et al., 1996], is critical for operational applications [Garg et al., 2022]. Due to the chaotic nature of the atmosphere system, determining the exact temperature at any given point in the future will always incur an error, especially for longer lead times. Because of this, it is more informative and useful to provide stakeholders with a wider range of possible prediction scenarios and their occurrence probability, as given by the model. This is even more relevant for extreme events, which are by definition rare and often missed by deterministic forecasts, especially at longer prediction horizons. For such high-impact situations, ensemble forecasting is widely recognized as a more powerful framework than deterministic prediction, as it better anticipates potential outcomes and supports decision-making under uncertainty, e.g., by enabling local authorities to take preventive measures to protect lives and infrastructure [Ponzano et al., 2025].

Earlier work on AIWP was clearly centered on deterministic weather forecasting due to the wide availability of data and benchmarks for such forecasts [Rasp et al., 2024]. However, there has recently been a growing body of work focused on probabilistic AIWP either by introducing post-hoc approaches akin to uncertainty quantification [Bülte et al., 2024], novel perturbation methods similar to those used in traditional NWP ensembles [Mahesh et al., 2025a], by applying Monte Carlo dropout [Garg et al., 2022] or training the model using a probabilistic objective through changes in the loss function [Lang et al., 2024a, Zhong et al., 2025, Alet et al., 2025], or by using generative diffusion AI models to directly produce probabilistic outputs [Price et al., 2024, Couairon et al., 2024]. Recent work suggests that the scarcity and imbalance of extreme events in training datasets can limit model generalization on tail events [Sun et al., 2025].

Uncertainty sources in a model can be divided into aleatoric uncertainty (originating from the source data, and by definition irreducible), and epistemic uncertainty (i.e. model-induced uncertainty) [Mucsányi et al., 2024]. This disentanglement is particularly challenging in the case of deep learning models, given that the training data itself is introducing uncertainty, at the same time as the architecture choices, training schedules, loss selection, and other hyperparameter tuning [Haynes et al., 2023].

Uncertainty quantification (UQ) can be done using post-hoc or following approaches based on initial conditions. Post-hoc methods rely on an established methodology to infer a probability distribution from a given deterministic model output. An example of such methods is the EasyUQ method [Walz et al., 2023]. While post-hoc methods are attractive in theory since they are simpler to implement, they make it

harder to disentangle sources of uncertainty in the model. Initial condition-based approaches involve making changes to the model input in some fashion and producing an ensemble of forecasts to infer a probabilistic distribution. To the authors’ knowledge, a systematic evaluation of how different AIWP models respond to perturbations has not yet been performed. While previous studies have explored techniques such as Bred Vectors [Baño-Medina et al., 2025b, Mahesh et al., 2025a], their study does not provide a comprehensive assessment across multiple architectures or perturbation strategies.

This paper aims to drive the discussion on the usage of AIWP models, specifically in the context of extreme weather forecasts, by comparing how different AIWP models respond to different input perturbation methods. With this aim, we hope to contribute to the following key research questions:

1. How can we create probabilistic weather forecasts from deterministic data-driven models?
2. How do different data-driven model architectures respond to uncertainty quantification?
3. Do AI-based ensembles demonstrate consistent predictive skill across diverse types of meteorological extremes?

By addressing these questions, our study seeks to advance the understanding of both the potential and the limitations of deterministic data-driven models in capturing extreme events through UQ. In order to achieve this, we will make use of two case studies: the 2022 Pakistan floods and the August 2022 China heatwave. We anticipate that the insights gained in this study will contribute to the practical deployment of data-driven models in operational settings.

## 2 Data

Two data sources are considered in this study: 1) ERA5 reanalysis data [Hersbach et al., 2020, Carver and Merose, 2023], which serves both as initial conditions for our forecasting models and as ground truth to evaluate the forecast performance; and 2) IFS, which is taken as a benchmark dataset to compare the forecast skill of the AIWP architectures with respect to the NWP models, represented by the ECMWF Integrated Forecasting System Ensemble (ENS) [Molteni et al., 1996, ECMWF, 2016]. We use a subset of the ERA5 ARCO [Carver and Merose, 2023] variables required for prediction and evaluation, following Bülte et al. [2024], with 6-hourly temporal resolution (see Table 1 for the complete list). To enable a fair comparison between the AIWP model and ENS outputs, all data used in this study are downscaled to a common  $1^\circ \times 1^\circ$  spatial resolution, using bilinear interpolation [Geneva and Foster, 2024]. The evaluation is conducted on: Geopotential at 500 hPa (**z500**), Temperature at 850 hPa (**t850**), 2 m Temperature (**t2m**) and Total Precipitation (6h accumulation, **tp06**), and additionally 24h aggregations for total precipitation ( $TP_{24h}$ ) and maximum 2 m Temperature ( $T2M_{24h}$ ).

## 3 Methodology

Figure 1 illustrates the methodology followed in this study. First, starting from ERA5 reanalysis data as initial conditions, we apply several perturbation methods, each of them generating  $M = 50$  different initial states. Then, these states are provided to diverse 6-hourly resolution AIWP models, resulting in  $M = 50$  different predictions, which constitute ensemble forecasting members for up to a 10-days lead time. The ensembles for all perturbation methods and AIWP models, along with ENS, are finally evaluated at daily resolution (accumulated precipitation or maximum daily temperature) against the ground-truth ERA5 to assess their forecasting capabilities.

For data handling and running predictions with various models, we use the NVIDIA-developed Earth2Studio framework [Geneva and Foster, 2024]. This modular and Python-based framework enables running large-scale inference, with multiple models and perturbation methods. In addition, for the evaluation of the forecasts, we make use of the WeatherBench framework [Rasp et al., 2024] and the probabilistic metrics extension to WeatherBench introduced in Zhao et al. [2025].

### 3.1 Models

We select three AIWP models for the purpose of this study that fulfill the following conditions:

1. Perform at/close to the state of the art for deterministic metrics for medium-range weather forecasting;

Table 1: ERA5 variables used for forecasting with AIWP models.

Variable	Description	Unit	Pressure levels (hPa)
<b>z (levels)<sup>a</sup></b>	Geopotential	$\text{m}^2 \text{s}^{-2}$	
<b>q</b>	Specific humidity	$\text{kg kg}^{-1}$	1000, 925, 850, 700,
<b>r<sup>b</sup></b>	Relative humidity	%	600, 500, 400, 300,
<b>t<sup>a</sup></b>	Temperature	K	250, 200, 150, 100,
<b>u<sup>a</sup></b>	U component of wind	$\text{m s}^{-1}$	50 (13 levels)
<b>v<sup>a</sup></b>	V component of wind	$\text{m s}^{-1}$	
<b>w</b>	Vertical velocity	$\text{Pa s}^{-1}$	
<b>msl<sup>a</sup></b>	Mean sea level pressure	Pa	
<b>u10m<sup>a</sup></b>	10m U component of wind	$\text{m s}^{-1}$	
<b>v10m<sup>a</sup></b>	10m V component of wind	$\text{m s}^{-1}$	
<b>u100m</b>	100m U component of wind	$\text{m s}^{-1}$	
<b>v100m</b>	100m V component of wind	$\text{m s}^{-1}$	
<b>t2m<sup>a</sup></b>	2m Temperature	K	
<b>d2m</b>	2m Dewpoint temperature	K	
<b>stl1</b>	Soil temperature level 1	K	
<b>stl2</b>	Soil temperature level 2	K	
<b>sp</b>	Surface pressure	Pa	
<b>tcwv</b>	Total column water vapour	$\text{kg m}^{-2}$	
<b>tcw</b>	Total column water	$\text{kg m}^{-2}$	
<b>swvl1</b>	Volumetric soil water layer 1	$\text{m}^3 \text{m}^{-3}$	
<b>swvl2</b>	Volumetric soil water layer 2	$\text{m}^3 \text{m}^{-3}$	
<b>tp06<sup>c</sup></b>	Total precipitation (6h accumulation)	m	
<b>z (surface)</b>	Geopotential at surface	$\text{m}^2 \text{s}^{-2}$	
<b>lsm</b>	Land-sea mask	(0-1)	
<b>sclor</b>	Standard deviation of orography	m	
<b>slor</b>	Slope of sub gridscale orography	m	

<sup>a</sup> This variable is perturbed when using perturbation methods. <sup>b</sup> This variable is derived from pressure, **q**, and **t**. <sup>c</sup> This variable is accumulated in 6-hourly intervals from the original 1-hourly data.

2. Have both model code and weights available in an open source way;
3. Produce forecasts for total precipitation and surface temperature, given that we want to understand the different models' prediction behavior concerning extreme precipitation and heatwaves, respectively.

Based on these criteria and our prior literature review, as well as taking into account diversity in model architecture type, this study uses three different architectures: FuXi [Chen et al., 2023b], GraphCast [Lam et al., 2023], and SFNO (Spherical Fourier Neural Operator) [Bonev et al., 2023]. For comparison, we also evaluated AIFSENS [Lang et al., 2024a], a probabilistically trained AIWP example model. Below, we summarize these models to highlight their architectures and forecasting approaches, referring the reader to their original publications for further details.

FuXi is a hybrid architecture combining a cascading U-Transformer with Swin Transformer V2 blocks to deliver high-accuracy forecasts across multiple time scales. FuXi uses three distinct sets of model weights to predict the weather between 0-5 days (FuXi short), 5-10 days (FuXi medium), and over 10 days (FuXi long) [Chen et al., 2023b]. As input, it takes two timesteps to predict the subsequent meteorological state ( $X^{t-1}, X^t \rightarrow X^{t+1}$ ).

GraphCast builds on the pioneering work of Keisler [2022] using a GNN based on an encoder, processor, and decoder architectures that include simultaneous multi-mesh message passing at different scales [Lam et al., 2023]. It relies on two timesteps as input to predict the following timestep ( $X^{t-1}, X^t \rightarrow X^{t+1}$ ), along with multiple forcing fields like time of day, day of year, and the total top of atmosphere incident solar radiation, among others. GraphCast has been trained on ERA5 data at  $1^\circ$  resolution and fine-tuned for IFS initial conditions at IFS-like resolutions ( $0.25^\circ$ ). We decided to make use of the  $1^\circ$  model for GraphCast in order to enable a fair comparison with all other models, which have not been finetuned on IFS initial conditions.

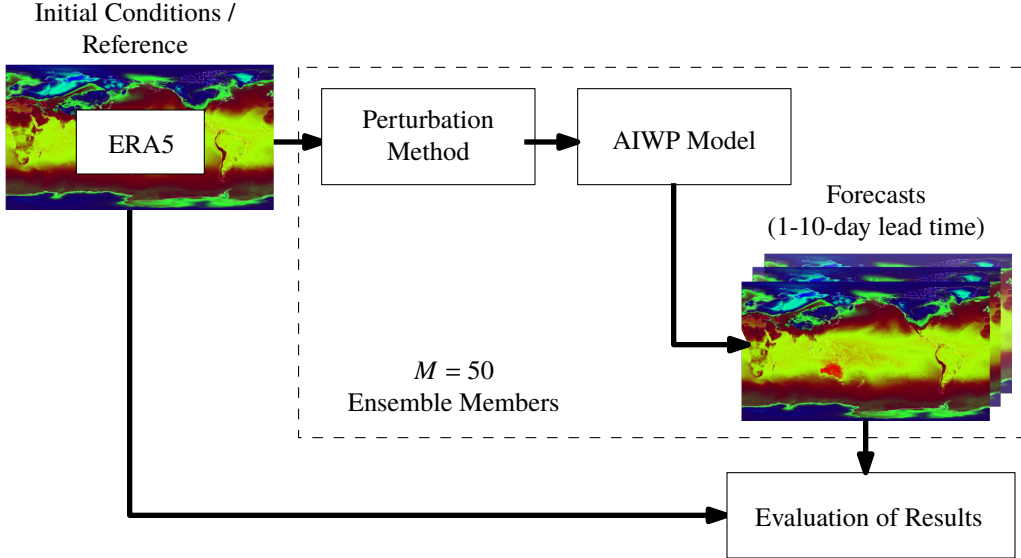


Figure 1: Overview of the study methodology, including the initial condition perturbation, forecasting with AIWP models, and evaluation of results stages.

SFNO is a Spherical Fourier Neural Operator-based architecture that is designed to leverage the properties of the Fourier operators on spherical geometries, modeling long-range dependencies in spatio-temporal data via convolutions [Bonev et al., 2023]. This model does not predict total precipitation directly, but comes with a trained diagnostic model [NVIDIA NGC Catalog, 2025] that takes in the output of the SFNO model and produces a total precipitation output ( $X^t \rightarrow X^{t+1}, \omega(X^{t+1})$ , where  $\omega$  is the diagnostic total precipitation model).

While this study focuses on three deterministic, state-of-the-art AIWP models, we acknowledge that other architectures could also have been included. In particular, models such as AIFS [Lang et al., 2024b] and Neural-GCM [Kochkov et al., 2024] represent important advances and improvements in forecast skill. Nevertheless, we believe that the selected set provides a representative cross-section of current state-of-the-art approaches across transformer-, GNN-, and operator-based architectures, allowing for a comparison of how leading AIWP models respond to input perturbations.

### 3.2 Perturbation Methods

We select three distinct perturbation methods for this study. The first, Gaussian noise, serves as a standard baseline. The second is the Hemispheric Centered Bred Vector (HCBV), drawing inspiration from Baño-Medina et al. [2025b]. The third method is HENS, inspired by the work of Mahesh et al. [2025a]. Both HCBV and HENS are variations of bred vectors, which are a class of flow-dependent, non-linear perturbations specifically designed to highlight and capture the most unstable modes of the underlying atmospheric flow [Feng et al., 2018, Toth and Kalnay, 1997].

#### 3.2.1 Gaussian Noise

The Gaussian perturbation method applies a random spherical Gaussian field, scaled with a fixed factor, to the input  $y$ . We used the Spherical Gaussian implementation in Geneva and Foster [2024]. Formally, it is expressed as follows:

$$y_{\text{pert}}[n] = y[n] + s \xi[n],$$

where  $n$  represents each input spatial location,  $s$  is the noise amplitude (scale factor), and  $\xi[n]$  is the mean-zero spherical Gaussian random field value sampled for each spatial location  $n$ .

### 3.2.2 Hemispheric Centered Bred Vector (HCBV)

The bred vector algorithm, firstly introduced in Toth and Kalnay [1993], is a perturbation method that is based on the fact that initial conditions generated by data assimilation/reanalysis processes accumulate growing errors. To estimate this growing error magnitude and direction, i.e., the bred vector  $\Delta f$ , the weather prediction model is used to create a perturbed forecast  $f_p$  based on a small change in the initial condition (seed). We use a hemispherical-centered approach [Mahesh et al., 2025a] where we scale the amplitude of  $\Delta f$  by a factor  $s$  and separately normalize the perturbation field in extra-tropical regions ( $|\text{latitude}| > 70^\circ$ ), i.e.  $\Delta f = s * \frac{f_p - f_u}{h(f_p - f_u)}$  (where  $f_u$  is the unperturbed forecast,  $h$  represents the hemispheric norm). We apply an integration factor of  $d = 3$ , following Baño-Medina et al. [2025a], recursively computing  $\Delta f$  three times to better sample the growing modes, which results in  $\Delta f_d$ . This is intended to more accurately reflect the uncertainties in the analysis data and data assimilation process. Moreover, we use a correlated spherical Gaussian noise for the 500 hPa geopotential variable as a seeding perturbation method ( $\Delta z_{500}$ ), with an amplitude of 1. The method is illustrated in Figure 2.

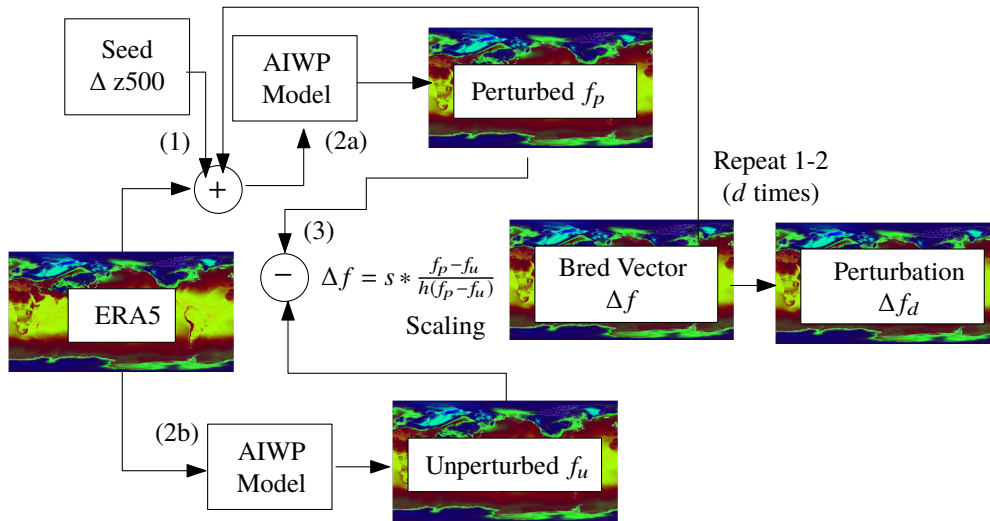


Figure 2: Hemispheric Centered Bred Vector (HCBV) perturbation method.  $\Delta z_{500}$  represents a correlated spherical Gaussian noise added to the 500 hPa geopotential variable.  $h$  represents the norm or size computed separately for the north and south hemispheres, and interpolated in the tropics.  $d$  represents the integration depth, that is, the number of recursive cycles from which the final perturbation is computed. This perturbation is additionally centered, so the perturbation vector is alternatively added and subtracted from the initial conditions. Diagram adapted from Baño-Medina et al. [2025b].

### 3.2.3 Huge Ensembles (HENS)

Huge ensembles (HENS) is a slightly adapted HCBV perturbation method [Mahesh et al., 2025a]. The method employs the global RMSE at 48h for each deterministic AIWP model and perturbed variable to further tune the amplitude of the perturbation ( $s_{HENS} = \text{RMSE}_{48h} * s$ ). The seed perturbation is also scaled using  $s_{HENS}$ . Similarly to HCBV, we use  $d = 3$  as a parameter for the integration depth [Baño-Medina et al., 2025b]. While an ensemble of model checkpoints is used in the original implementation of HENS to produce the final ensemble prediction, we only use the HENS input perturbation method in this study.

It should be noted that only the common input variables between all models are perturbed (see Table 1). Moreover, we use a scaling factor  $s = 0.35$  for all perturbation methods, following Mahesh et al. [2025a].

### 3.3 Evaluation Metrics

We select three complementary evaluation metrics: 1) the well-known **RMSE** as a deterministic score; 2) the Continuous Ranked Probabilistic Score (**CRPS**), which constitutes an overall probabilistic score; and 3)

the Receiver Operating Characteristic Skill Score (**ROCSS**), a probabilistic score tailored to extremes. The reader is referred to Appendix A for comprehensive metric definitions.

#### 4 Case studies

Two case studies are considered for this study: the Pakistan Floods and the China Heatwave in August 2022. They are illustrated in Figure 3. For our purposes, only data within the geographical bounds displayed in the figure and corresponding to August 2022 is used. For both the Pakistan floods and the China heatwave, we use the climatological 99th-percentile threshold to isolate and define the extremes, consistent with precipitation analyses in Singh et al. [2024] and heatwave characterizations in Sun et al. [2021].

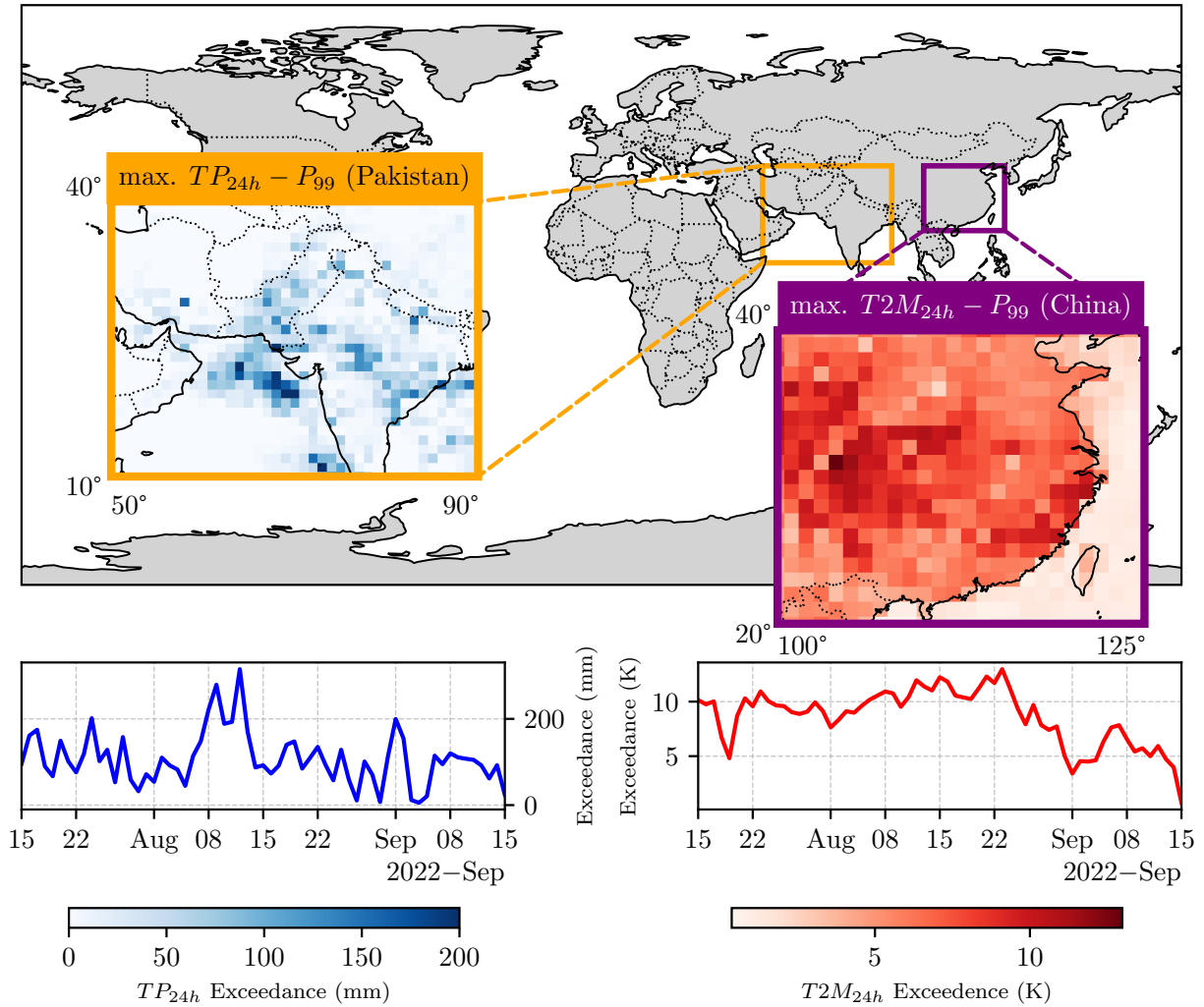


Figure 3: Analysis of the August 2022 Pakistan extreme precipitation and China heatwave, based on ERA5. The values displayed (in the spatial and temporal dimensions) correspond to the exceedance of the 99th percentile of the ERA5 1990-2020 climatology for daily total precipitation and daily maximum temperature. The geographical bounds of each case study are also shown. A maximum of 200 mm of precipitation exceedance can be appreciated in Pakistan, while a sustained 10 K exceedance over August is observed in China, further reinforcing the extreme nature of both these events.

#### 4.1 Summer 2022 Pakistan Floods

In the summer of 2022, Pakistan experienced catastrophic flooding that submerged one-third of the country, resulting in over 1000 deaths, displacing 30 million people, and causing over 30 billion USD in damages [Arshad et al., 2025]. The rainfall observed in this period was four standard deviations above the climatological mean and twice the amount of a previous flooding event in 2010 [Hong et al., 2023]. Recent studies have linked this extreme event with concurrent heatwaves [Hong et al., 2023], which favored snow melt, subsequently followed by extreme precipitation [Shehzad, 2023]. During that time, parts of the territory experienced daily precipitation amounts above 100 mm, which, according to Ikram et al. [2016], is considered extreme in Pakistan. Large parts of Pakistan with daily precipitation exceeding 100 mm can be observed in Figure 3 corresponding to the 99th percentile of the 1990-2020 climatology of daily precipitation during August 2022.

#### 4.2 August 2022 China Heatwave

During August 2022, southern China was hit with a record-breaking heatwave, with over 360M people experiencing temperatures above 40° C [Gong et al., 2024]. This heatwave represented the greatest anomaly since 1979, caused severe impact, including massive droughts [Zhou et al., 2023, Sun et al., 2023]. As can be seen in Figure 3, the region presented close to 10° C exceedance with respect to the 99th-percentile of the ERA5 1990-2020 climatology for daily maximum temperature in the majority of days in August 2022, with an even greater exceedance in the Sichuan Basin.

### 5 Results

We begin this section by evaluating the performance of the three selected deterministic AIWP models in predicting extreme events under input perturbations. The resulting ensembles exhibited varying skill depending on the predicted variable, model architecture, perturbation strategy, and forecast lead time. In the following figures we analyze the ROCSS for each case study, inspect the spatial spread characteristics, and, finally, analyze the tail density distribution. In addition, we explore the links between the performance in these case studies and global evaluation metrics like CRPS and RMSE.

Figure 4 summarizes the ROCSS at the 99th-percentile for daily precipitation over Pakistan and daily maximum temperature over China. Overall, ensemble skill decreases with lead time (with the exception of SFNO for precipitation), reflecting the limited predictability horizon of these AIWP and NWP systems. For both ENS and AIFSENS, we notice a slight increase in performance for precipitation from 1 to 2 lead times, most likely due to the fact that ENS is initialized with IFS initial conditions and AIFSENS is also fine-tuned with that data, which causes a small dip in performance in the first forecast step when compared with models trained with ERA5. However, both ENS and AIFSENS showcase the best metrics across variables and lead times, with AIFSENS showing significantly higher ROCSS than ENS up to a 5-day lead time for precipitation and a 7-day lead time for temperature, demonstrating the benefits of probabilistically trained models. Among the perturbation methods, HENS consistently achieved the highest probabilistic skill on these extreme events, followed by HCBV and the Gaussian perturbation, and all perturbations methods improved upon the model’s deterministic skill.

For very high precipitation in Pakistan, GraphCast–HENS reaches ROCSS  $\approx 0.83$  at lead time of 1 day (the only precipitation metric showing a significantly higher ROCSS than ENS), which is higher than GraphCast–Gaussian (0.76), and maintains ROCSS above 0.6 through a lead time of 5 days. In contrast, SFNO ensembles exhibit weak discrimination skill for extreme precipitation (ROCSS  $< 0.34$ ), indicating very limited performance for precipitation extremes. Interestingly, the performance for SFNO overall decreases around a 4-5-day lead time and recovers to its highest values around a 10-day lead time for HENS perturbations. SFNO uses a separate diagnostic model to produce precipitation forecasts. This diagnostic model was trained using ERA5 data [NVIDIA NGC Catalog, 2025], not SFNO forecasts, which could potentially explain the poor performance of SFNO for precipitation.

For temperature extremes in China, SFNO–HENS performs best, attaining ROCSS  $\approx 0.93$  at a lead time of 1 day, nearly matching AIFSENS (0.95), and being significantly higher than ENS up to a 7-day lead time. FuXi–Gaussian shows the worst performance, and it is the only model that does not show significantly higher ROCSS than ENS at any lead time.

Interestingly, HENS perturbations support GraphCast ROCSS for longer lead times for precipitation than FuXi, which very precipitously decreases performance across lead times, reaching a minimum ROCSS from 0.77 to 0.19. In addition, for all models, ROCSS for temperature is comparatively much more stable across

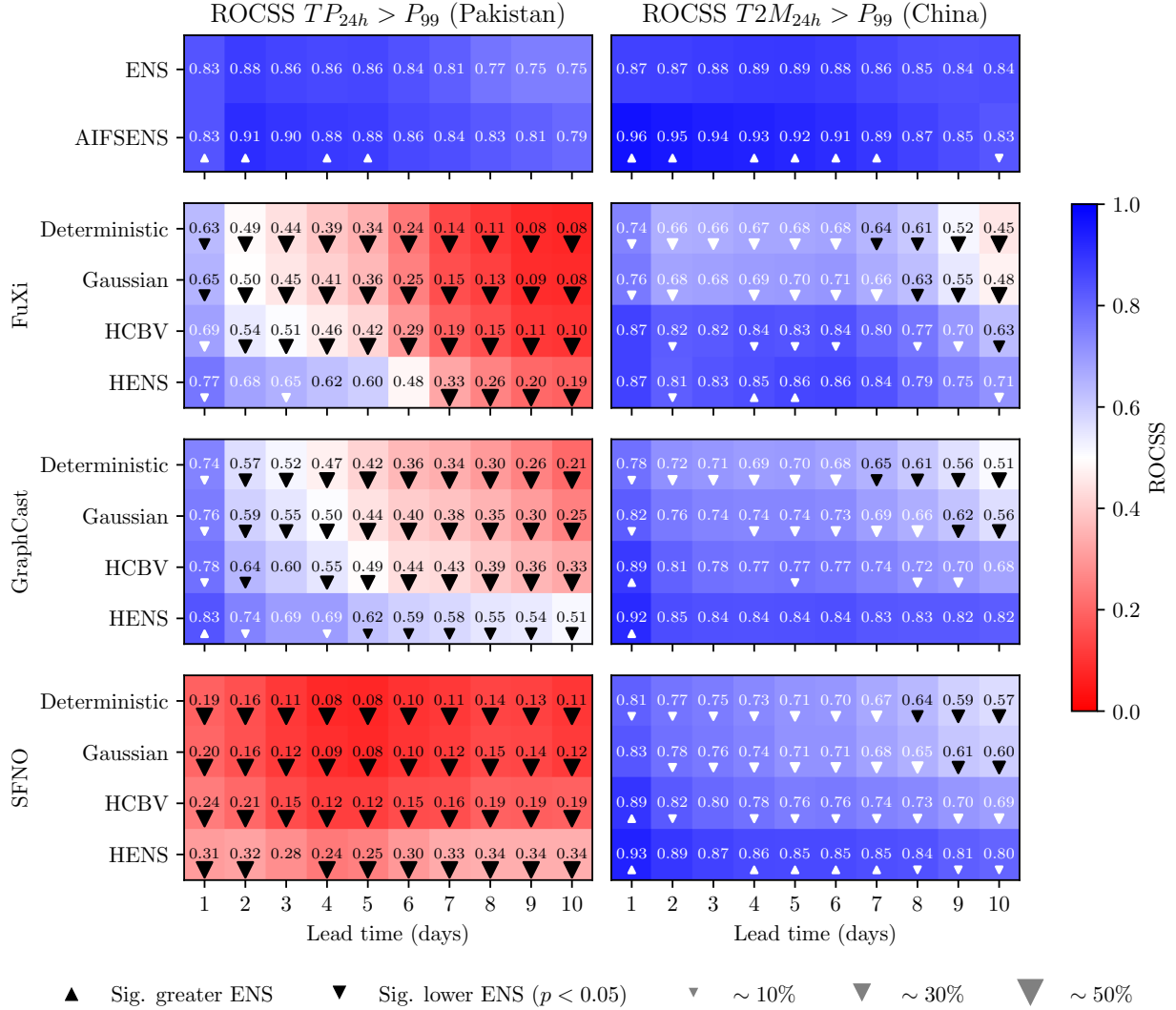


Figure 4: ROCSS values at the 99th percentile of the ERA5 1990-2020 climatology for daily accumulated precipitation ( $TP_{24h}$ ) and maximum daily temperature ( $T2M_{24h}$ ), across 10 lead times, for the different AIWP models and their ensembles, and the Pakistan and China region in August 2022. The symbols under the values represent significantly higher or lower differences in the metric compared with ENS ( $p < 0.05$ ), while the symbol size represents the magnitude of the difference. The higher the ROCSS values, the better the performance on the extremes. HENS perturbations achieve the highest ROCSS across all models ensembles.

lead times. This pattern suggests that AIWP models are more effective at representing uncertainty in smoother, large-scale thermodynamic fields than in localized precipitation fields.

The spatial ensemble spread at 3-day lead time in Pakistan (Figure 5) and China (Figure 6) highlights important structural differences between AIWP perturbed ensembles, ENS, and AIFSENS. In Figure 5, we can observe that ENS and AIFSENS capture the heavy precipitation core and associated uncertainty. The perturbed AIWP ensembles generally remain under-dispersive, although FuXi-HENS exhibits the most similar spatial variance structure, partially recovering the high-spread region over southern Pakistan. Gaussian perturbations seem to create almost no ensemble spread regardless of the model used.

During the China heatwave, both ENS and AIFSENS showcase similar spatial patterns and intensity for the ensemble spread, as illustrated in Figure 6. Notably, the very high temperature region in the Sichuan Basin, where the highest temperature of  $\approx 45$  °C is observed in ERA5, is not particularly high in ensemble spread for our reference forecasts (ENS and AIFSENS). Among AIWP perturbed ensembles, FuXi-HENS

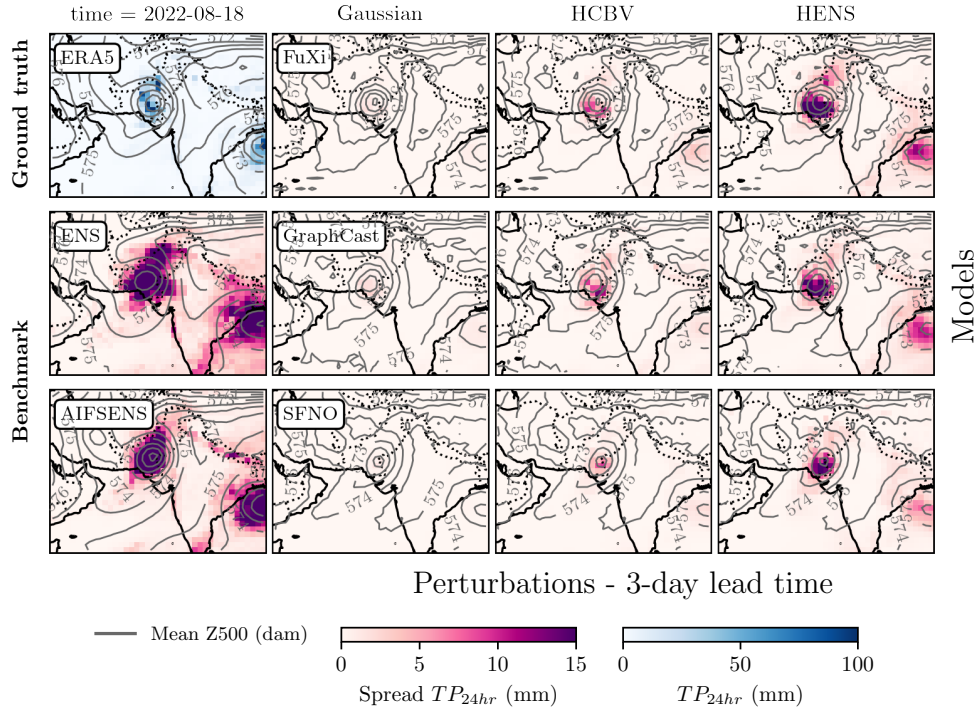


Figure 5: Daily accumulated precipitation spread for the different ensemble models (ENS, AIWPs) over Pakistan on 18th August 2022 for a 3-day lead time forecast. Ground-truth ERA5 spatial distribution for daily precipitation is shown in the top left corner. Daily average geopotential height at 500 hPa is also displayed as contour lines.

and SFNO–HENS provide the closest approximation in ensemble spread, aligning their spread maxima with ENS. GraphCast ensembles capture large-scale gradients but underestimate ensemble spread amplitude. FuXi–HCBV produces a spatially irregular pattern in the ensemble spread, which is unique in our perturbation set. That can reflect a low-amplitude collapse of the bred vectors [Toth and Kalnay, 1997], since the seed perturbation factor of HCBV applied onto z500 is 1 while for HENS it is around 30 (i.e. the z500 RMSE at 48h for FuXi). This occurs specifically for FuXi and surface temperature, potentially due to its relative sensitivity to input changes in surface temperature. Zhong et al. [2025] identified ensemble spread underestimation for this probabilistically trained FuXi variant, which could point to limitations in the base architecture itself. As seen in Figure 5, Gaussian perturbations are clearly under-dispersive.

The tail distributions of ensemble forecasts for precipitation (Figure 7) and temperature (Figure 8) reveal systematic differences in how the different AIWP models represent these extreme events across lead times, and how different perturbations have a comparatively small impact on the distribution density on the tails. For precipitation over Pakistan in Figure 7, comparing ENS and AIFSENS, ENS seems to be slightly left-skewed, underrepresenting the density of high precipitation values in comparison with AIFSENS, which almost perfectly follows ERA5, especially at short lead times. FuXi shows the biggest difference between tail density representation along the lead times, which can be due to its cascading approach along lead time horizons [Chen et al., 2023b]. GraphCast appears to best capture the ERA5 tail representation out of our AIWP perturbed ensembles, which is in agreement with the better ROCSS in Figure 4. For SFNO, there is a larger density underestimation (distribution is left-skewed overall). The longer the lead time (9 days), the closer the density is to ERA5, which concurs with the dip and rise ROCSS we observed for SFNO–HENS for precipitation. The perturbation HENS seems to have a smoothing effect over the estimated density across models and perturbations.

Figure 8 shows the ensemble tail distribution for the China heatwave. At a 1-day lead time, AIFSENS almost perfectly follows the ERA5 estimated density, consistent with the pattern observed for precipitation. SFNO–HENS closely reproduces the warm-tail behavior ( $> 305$  K) at short lead times being comparable to AIFSENS, which explains the high ROCSS observed in Figure 4. At longer lead times (9 days), all models,

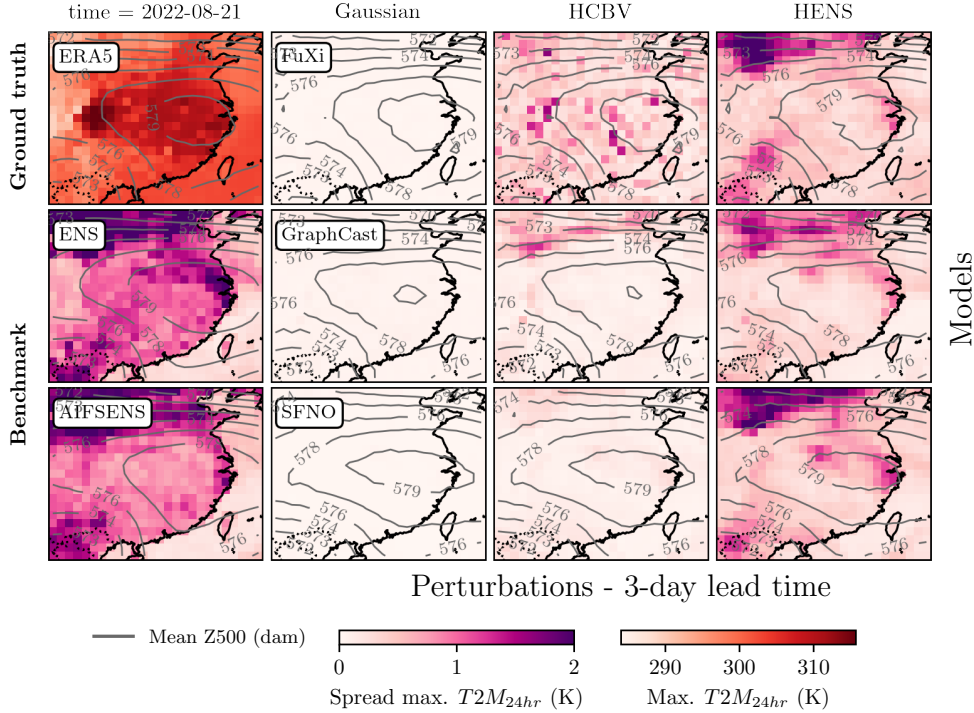


Figure 6: Daily maximum temperature spread for the different ensemble models (ENS, AIWPs) over China on 21st August 2022 for a 3-day lead time forecast. Ground-truth ERA5 spatial distribution for maximum temperature is shown in the top left corner. Daily average geopotential height at 500 hPa is also displayed as contour lines. AIFSENS closely matches the ENS spread, while FuXi–HENS comes closer from the perturbed ensembles.

including ENS and AIFSENS (except SFNO), seem to be left-skewed, struggling to represent the extreme density distribution. Both GraphCast and FuXi, at shorter lead times (1-5 days), seem to overestimate smaller extreme values (between 305 K and 310 K), at the detriment of higher extreme values. HENS appears to showcase the same smoothing of the density behavior as observed in the precipitation example, indicating a unified effect of the HENS perturbation on the distribution representation.

We further assess global performance to determine whether the patterns observed in these case studies extend across all regions, and non extreme settings. Globally averaged metrics reinforce the regional findings (see Appendix B). HENS perturbations yield the lowest CRPS and ensemble spreads most consistent with the ENS benchmark (see Figures 9 and 10). Gaussian perturbations produce overly tight ensembles (under-dispersion), while HCBV perturbations improve the model spread, but remain under-amplified. As expected, probabilistic skill is consistently higher for temperature than for precipitation across all models.

For both case studies and global evaluations, the results reveal a consistent pattern: flow-dependent perturbations, particularly the HENS method, most effectively enhance ensemble realism and probabilistic skill among deterministic AIWP models. Overall, ensemble skill (ROCSS, CRPS) declines with forecast lead time, reflecting the inherent limits of predictability and the growing influence of model-driven uncertainty. HENS perturbations yield broader, better-calibrated spreads and tail distributions closer to ERA5, compared to Gaussian or HCBV, narrowing the performance gap with ENS and AIFSENS, though not closing it. FuXi and GraphCast respond to perturbations and retain competitive deterministic accuracy up to 3–5 days, while SFNO remains under-dispersive and insensitive to perturbations for precipitation. AIWP models perform substantially better for temperature extremes (coherent, large-scale events) than for precipitation extremes, which depend on small-scale convective processes poorly represented in their training data. Globally, CRPS and RMSE metrics confirm that perturbation-based ensembles can emulate aspects of probabilistic behavior, but still lack the spatial variability and multiscale energy structure of NWP ensembles. Overall, while HENS moves AIWP deterministic models toward meaningful ensemble forecasting, performance mismatches persist.

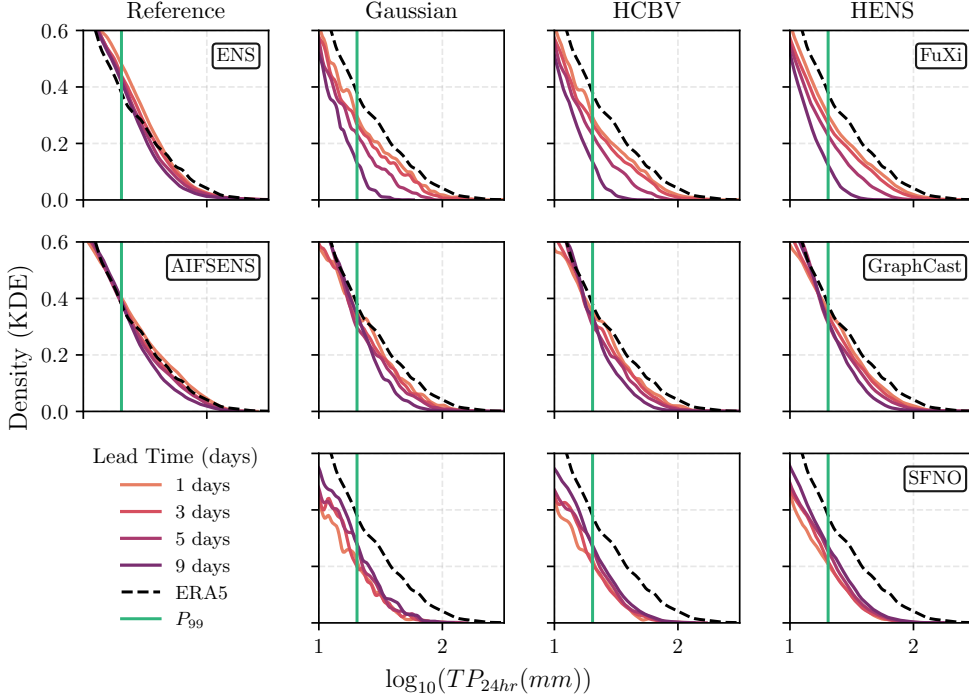


Figure 7: Tail distribution density (computed using Kernel Density Estimation) of 24-hour accumulated precipitation over the Pakistan region in August 2022, given the different models ensembles and the reference ENS and AIFSENS forecasts. Note that only values where  $TP_{24h} > 1$  mm are used to compute the density estimations.

## 6 Discussion

Our findings are broadly consistent with recent evaluations of deterministic AIWP models [Olivetti and Messori, 2024, Zhang et al., 2025, Brenowitz et al., 2024], which report that data-driven systems outperform traditional NWP in deterministic metrics, but exhibit weaker probabilistic skill. Similar to Mahesh et al. [2025a,b], we observe that perturbation-based ensembles can create meaningful spread from AIWP architectures. Indeed, the superior performance of the HENS and HCBV methods supports the notion that perturbations aligned with atmospheric error-growth directions (e.g., bred vectors) are more effective than Gaussian noise, which had already been reported by Bülte et al. [2024] when comparing with Random Field Perturbations. In this study, we have found GraphCast to have an advantage for precipitation, which can point to the benefits of using a graph-based representation of the atmosphere. SFNO performs best for temperature, which highlights the Fourier neural operator’s ability to represent large-scale thermodynamic fields.

Preliminary analysis of the ensemble power spectra indicates that all AIWP ensembles underestimate the variance of ensemble spread at all scales, compared with the ENS benchmark (see Appendix C). When inspecting the spectra of the deterministic models’ forecast, we can see that, for surface temperature, the spectra are very close to ERA5, with the AI models dropping in power at the mesoscale (blurring). For total precipitation, SFNO stands out as underpowered at all scales, while the other AI models up until 3-day lead-time seem to accompany the power spectrum of ERA5 more closely than ENS. This is in line with findings from Rodwell et al. [2025], where smaller-scale variance (and forecast error) is present in AIWP models at longer lead times, specifically for AIFSENS.

Spatial comparison of ensemble spreads (see Figures 5 and 6) confirms that AIFSENS most closely matches ENS variability, while FuXi HENS narrows this gap, suggesting that perturbation ensembles can approximate observational uncertainty when using deterministic models. However, specifically for precipitation, there are known limitations of ERA5 for capturing spatial variability, especially in the tropics [Lavers et al., 2022]. Further work could explore ensembles evaluated on ground station data or regional reanalysis, which may provide a more faithful representation of the precipitation pattern [Gupta et al., 2025].

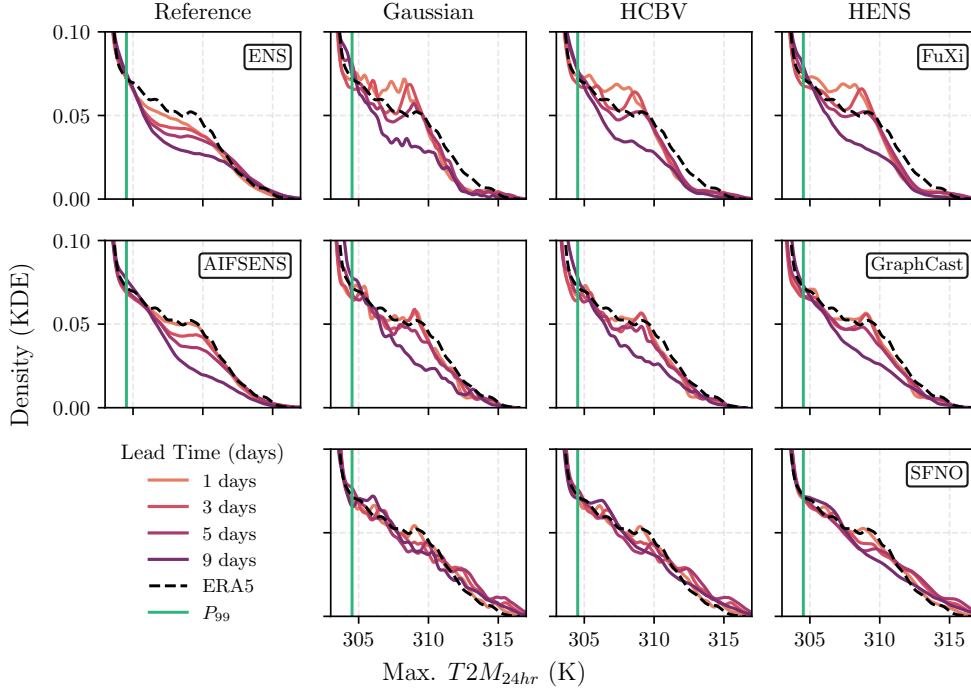


Figure 8: Tail distribution density (computed using Kernel Density Estimation) of 24-hour maximum 2 m temperature over the China region in August 2022, given the different models ensembles and the reference ENS and AIFSENS forecasts. Only values where  $T2M_{24h} > 300$  K are used to compute the density estimations.

The decline in ensemble skill with lead time reflects two interacting uncertainty sources: sensitivity to initial conditions (aleatoric uncertainty) and model-induced (epistemic) uncertainty. Our experiments isolate the first component (aleatoric) through input perturbations, yet beyond a lead time of 5 days, all models converge in global performance. This implies that epistemic uncertainty stemming from architectural bias, loss formulation, and underrepresented physical feedback becomes the controlling factor at longer lead times. Combining both input perturbations and model checkpoint ensembles has been shown to provide high probabilistic skill and a better overall uncertainty representation [Mahesh et al., 2025a, Baño-Medina et al., 2025b]. Still, obtaining multiple model checkpoints from already trained models or producing very large numbers of ensembles is computationally expensive. Further study could explore alternative ways to add model stochasticity, as well as their impact on the performance at the extremes.

Ensembles from FuXi and GraphCast maintain a global CRPS comparable to or better than ENS for temperature up to 3–5 days, but performance degrades more quickly for precipitation. The contrast between temperature and precipitation skill suggests that predictive performance is hindered not only by the rarity of the event but also by the physical nature of the target variable, which had been previously reported [Zhao et al., 2025]. Temperature extremes are often spatially coherent and governed by persistent synoptic features [Yang et al., 2020], which AIWP models capture well. Precipitation extremes, in contrast, depend on subgrid processes that are underrepresented in training data [Hess and Boers, 2022]. With that, extreme event prediction difficulty reflects both data imbalance and process complexity. Improving AIWP generalization for rare hydro-meteorological extremes may require targeted loss weighting, balanced sampling, or training with precipitation specific datasets [Sun et al., 2025, Hess and Boers, 2022].

Our case studies also reveal that model performance differences are not purely regional but depend on feature representation. For instance, while the FuXi ensemble showed a high skill to capture the China heatwave, it showed a lower performance for the monsoon-driven precipitation in Pakistan. This suggests that evaluating AIWP ensembles on a feature basis linked to atmospheric regimes or teleconnection patterns could yield more diagnostic insight than regional averages. Future work could categorize ensemble skill by dynamic regime (e.g., subtropical high, monsoon trough) to distinguish model sensitivity to specific atmospheric features. At the same time, this study focuses only on a small time scale and geographical region. A natural extension to this work would be applying the same methodology to other time scales and regions, adding, for instance,

seasonal variability. In addition, the coarse resolution used in this study ( $1^\circ$ ) could also negatively affect the reported performances, especially for precipitation [Hess and Boers, 2022].

The 2022 Pakistan extreme precipitation and China heatwave were physically connected through large-scale Rossby wave propagation [Hong et al., 2023]. Despite being treated as separate regional events in this study, their concurrent occurrence, and the difference in performance we encountered between the two case studies can point to the inability of AIWP models to represent compound extremes spanning distant regions. This highlights a frontier for probabilistic AIWP systems to represent not just local extremes, but their compound and causal linkages across regions.

Overall, our results show that while deterministic AI weather models can approximate aspects of probabilistic behavior through input perturbations, specifically flow-dependent perturbations like bred vectors, they still fall short of fully capturing uncertainty and extremes. The HENS method offers a promising bridge toward more realistic ensemble forecasts, getting closer to the performance of traditional NWP systems. Future research could focus on integrating flow-dependent perturbations with generative or latent-space approaches, improving training data for extremes or exploring multi-model ensembles.

## 7 Conclusions

This study evaluated how deterministic AIWP models respond to input perturbations and how their resulting ensembles represent uncertainty during extreme events. Using FuXi, GraphCast, and SFNO, we generated 50-member ensembles with Gaussian, HCBV, and HENS perturbations, applied to the 2022 Pakistan floods and China heatwave. This constitutes the first systematic comparison of ensemble generation techniques for deterministic AI weather models. Our findings show that flow-dependent perturbations, particularly HENS, produce the most skillful and realistic ensembles, outperforming Gaussian noise and narrowing the performance gap with NWP (ENS) and native probabilistic AIWP models such as AIFSSENS. While all AIWP models captured temperature extremes more reliably than precipitation, their probabilistic skill declined with lead time, indicating a transition from initial-condition (aleatoric) to model-driven (epistemic) uncertainty. Overall, perturbation-based ensembles extend deterministic AI models toward operational probabilistic forecasting. However, fully capturing the uncertainty and multiscale dynamics of extreme events could require hybrid strategies that integrate flow dependent perturbations with noise added to the latent-space or generative approaches, improved training on rare extremes, or multi-model ensemble frameworks. Advancing along these directions will be key for building trustworthy, AI-driven early warning systems for high-impact weather events.

## Acknowledgments

This research has been supported by the European Union’s Horizon Europe research and innovation program (EU Horizon Europe) project MedEWSa under grant agreement no. 101121192. M.-Á. F-T thanks the support of the grant for mobility stays from the Research and Transfer Program of Universidad Carlos III de Madrid, Spain, and acknowledges the computer resources provided by Artemisa, funded by the ERDF and Comunitat Valenciana, as well as the technical support provided by the Instituto de Física Corpuscular, IFIC (CSIC-UV).

## Data availability statement

The ERA5 data in this study was obtained using the ERA5 ARCO dataset hosted on Google Cloud <https://github.com/google-research/arco-era5>. The IFS ENS data in this study was obtained from the WeatherBench 2 dataset <https://weatherbench2.readthedocs.io/en/latest/data-guide.html>. The code for processing the data, running the perturbations, and computing the metrics can be found in <https://gitlab.hhi.fraunhofer.de/ai-aml/aiwpuq>.

## A Evaluation Metrics and Statistical Significance Testing

For the following metric definitions,  $y_{nt}$  is the ERA5 value for each spatial location  $n$  ( $N$  spatial locations in a study region) at time  $t \in \{1, \dots, T\}$ , being  $T$  the number of forecast timesteps, and  $\hat{y}_{nt}^{(m)}$  is the forecast provided by an ensemble member  $m \in \{1, \dots, M\}$ , where  $M = 50$ .

### A.1 Root Mean Squared Error (RMSE)

The Root Mean Squared Error (RMSE) is a metric that measures the average magnitude of errors between predicted and observed values [Rasp et al., 2024]. It penalizes larger errors more heavily, making it sensitive to outliers. Lower RMSE represents a better forecast. RMSE is defined as follows:

$$\text{RMSE} = \sqrt{\frac{1}{NT} \sum_{n=1}^N \sum_{t=1}^T \left( y_{nt} - \frac{1}{M} \sum_{m=1}^M \hat{y}_{nt}^{(m)} \right)^2}$$

### A.2 Continuous Ranked Probability Score (CRPS)

The Continuous Ranked Probability Score (CRPS) is a scoring rule that measures the accuracy of probabilistic forecasts by quantifying the difference between the predicted cumulative distribution function (CDF) and the observed outcome [Rasp et al., 2024]. It generalizes the mean absolute error to probabilistic forecasts. Lower CRPS points at better forecast skill. CRPS is defined as follows:

$$\text{CRPS} = \frac{1}{NT} \sum_{n=1}^N \sum_{t=1}^T \left[ \frac{1}{M} \sum_{m=1}^M \left| \hat{y}_{nt}^{(m)} - y_{nt} \right| - \frac{1}{2M^2} \sum_{m=1}^M \sum_{k=1}^M \left| \hat{y}_{nt}^{(m)} - \hat{y}_{nt}^{(k)} \right| \right]$$

### A.3 Receiver Operating Characteristic Skill Score (ROCSS)

The Receiver Operating Characteristic Skill Score (ROCSS) is a metric derived from the Area Under the ROC Curve (AUC) that quantifies the ability of a forecasting system to discriminate between the occurrence and non-occurrence of an event, relative to random chance [Zhao et al., 2025].

We set the event threshold  $\tau$  to the 99th climatological percentile from ERA5 (1990–2020) to capture the extremes relevant to this study. The 2022 Pakistan floods were a record-breaking precipitation event [Singh et al., 2024], warranting a high percentile threshold to isolate tail behavior. For heat extremes in China, the 99th percentile aligns with established heatwave-impact studies such as Sun et al. [2021], where severe heatwave conditions are characterized using upper-percentile exceedance. Together, these justify the choice of  $\tau = P_{99}$  as an appropriate discriminator for rare, high-impact extremes.

The computation of the ROCSS proceeds as follows:

1. Thresholding observations and ensemble forecasts: Given the threshold  $\tau$ , observations and ensemble forecasts are converted into binary outcomes. Then, ensemble binary forecasts are converted into forecast probabilities:

$$o_{nt} = \mathbf{1}\{y_{nt} > \tau\}, \quad f_{nt}^{(m)} = \mathbf{1}\{\hat{y}_{nt}^{(m)} > \tau\}, \quad r_{nt} = \sum_{m=1}^M f_{nt}^{(m)}, \quad p_{nt} = \frac{r_{nt}}{M+1}.$$

Here,  $o_{nt}$  is the binary observation,  $f_{nt}^{(m)}$  is the binary forecast of ensemble member  $m$ ,  $r_{nt}$  is the ensemble “vote count” and  $p_{nt}$  is the resulting forecast probability using Weibull’s plotting position [Weibull, 1939].

2. Applying probability thresholds: To construct the ROC curve, the forecast probability is converted back to binary outcomes for each probability threshold  $\theta \in [0, 1]$ :

$$\hat{o}_{nt}(\theta) = \mathbf{1}\{p_{nt} \geq \theta\}$$

3. Calculating Hit Rate (HR) and False Alarm Rate (FAR):

$$\text{HR}(\theta) = \frac{\sum_{n,t} \mathbf{1}\{\hat{o}_{nt}(\theta) = 1 \wedge o_{nt} = 1\}}{\sum_{n,t} o_{nt}}, \quad \text{FAR}(\theta) = \frac{\sum_{n,t} \mathbf{1}\{\hat{o}_{nt}(\theta) = 1 \wedge o_{nt} = 0\}}{\sum_{n,t} (1 - o_{nt})}.$$

4. Constructing the ROC curve: The ROC curve plots the trade-off between hits and false alarms across all probability thresholds:

$$\{(\text{FAR}(\theta), \text{HR}(\theta)) : \theta \in [0, 1]\}$$

5. Computing the AUC:

$$\text{AUC}_{\text{forecast}} = \int_0^1 \text{HR}(\text{FAR}^{-1}(x)) dx,$$

where  $\text{FAR}^{-1}(x)$  denotes the inverse mapping of the false alarm rate along the ROC curve.

6. Computing the ROCSS: Finally, the ROCSS compares the forecast AUC to a reference (random) forecast, which has  $\text{AUC}_{\text{reference}} = 0.5$ :

$$\text{ROCSS} = \frac{\text{AUC}_{\text{forecast}} - \text{AUC}_{\text{reference}}}{1 - \text{AUC}_{\text{reference}}}.$$

A higher ROCSS indicates better discriminatory skill, with 1 representing perfect skill and 0 corresponding to no skill.

#### A.4 Statistical Significance Testing

To assess whether the differences in model performance between AIWP model ensembles and ENS, specifically in ROCSS, are statistically significant, we employ a clustered panel  $t$ -test based on a panel regression framework, following Olivetti and Messori [2024].

For each variable (daily accumulated precipitation,  $TP_{24h}$ , and maximum daily temperature,  $T2M_{24h}$ ) and forecast lead time, we first compute the difference in ROCSS between the AIWP model ensemble and ENS at each grid cell and validation date. The resulting dataset (`diff`) is structured as a panel with spatial and temporal dimensions, indexed by latitude and longitude coordinates and valid time:

$$\text{diff}_{nt} = y_{nt},$$

where  $n$  denotes the spatial location (grid point) and  $t$  the time index (validation date). We then estimate the following panel model:

$$y_{nt} = \alpha + \varepsilon_{nt},$$

where  $\alpha$  represents the mean difference in ROCSS between the AIWP model ensemble and ENS, and  $\varepsilon_{nt}$  is the error term. The model is fit with two-way clustered standard errors, accounting for correlation within both spatial entities (grid cells) and across time. From the fitted model, we extract the  $t$ -statistic associated with the intercept ( $\alpha$ ), representing whether the mean difference significantly differs from zero.

Significance thresholds are determined from the Student's  $t$  distribution with degrees of freedom equal to the number of panel observations. Differences are classified as statistically significant at the 5% level ( $p < 0.05$ ) when the  $t$ -statistic exceeds these bounds. The `PanelOLS` implementation from the `linearmodels` Python package is used to perform the computations.

## B Global RMSE and CRPS for August 2022

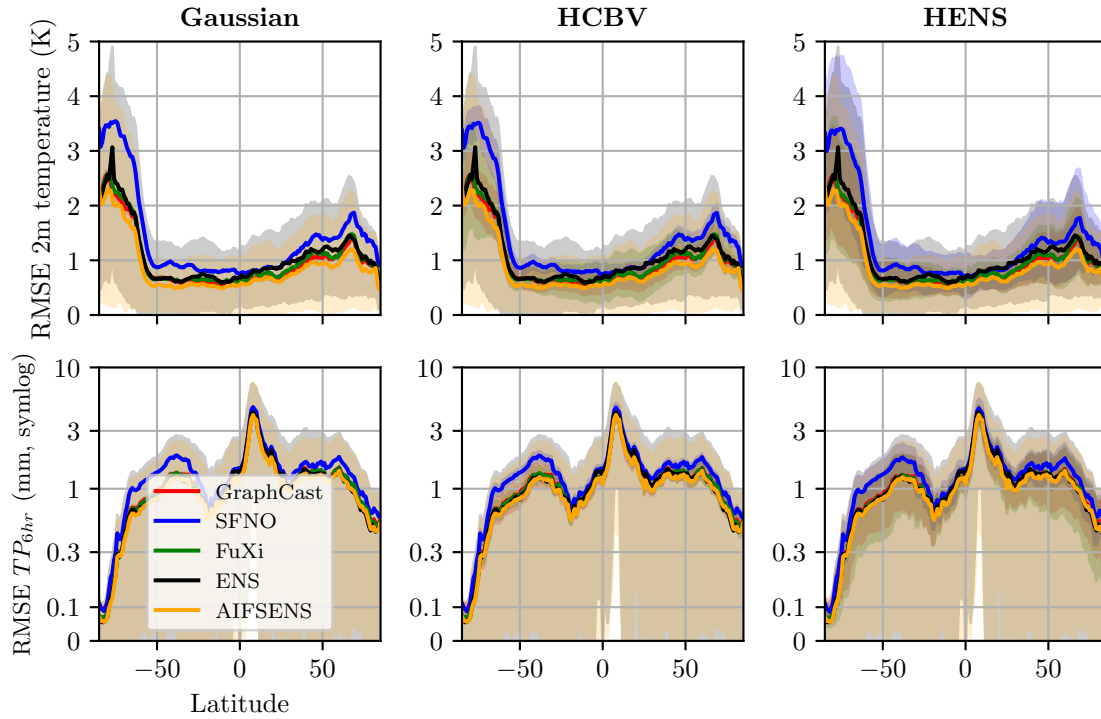


Figure 9: Ensemble mean RMSE per latitude for a 3-day lead time worldwide forecast in August 2022. The shaded area represents the ensemble mean RMSE variance. The Gaussian perturbation method provides under-dispersive ensembles. The HENS method most closely matches the ENS spread. SFNO performs worse on all variables and perturbation methods, while GraphCast and FuXi perform at a similar level, but still not reaching the dispersion of ENS.

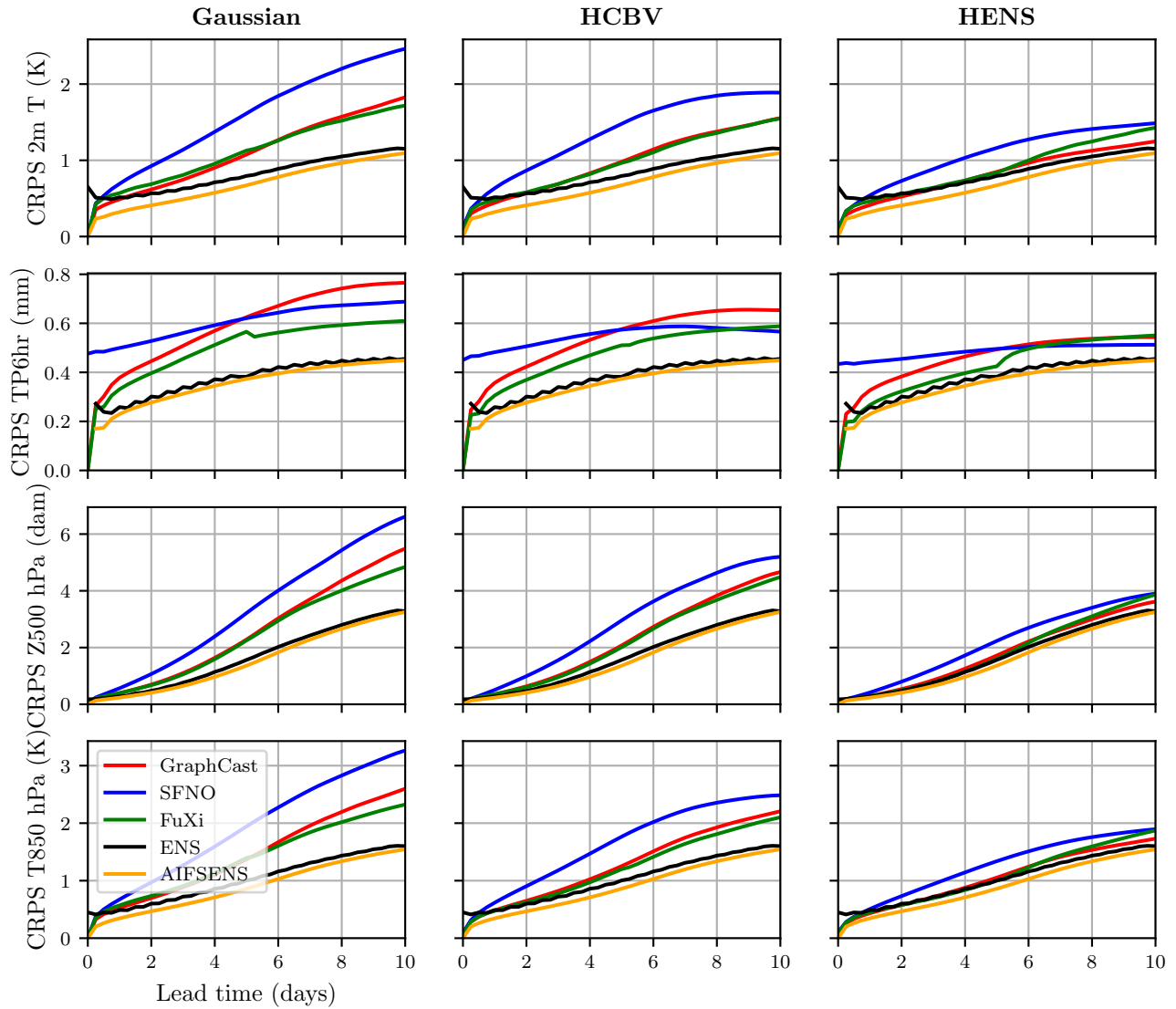


Figure 10: Global average CRPS over 10-day lead time for the different perturbation methods and AIWP models and ENS, in August 2022.

### C Power Spectra of Forecasts

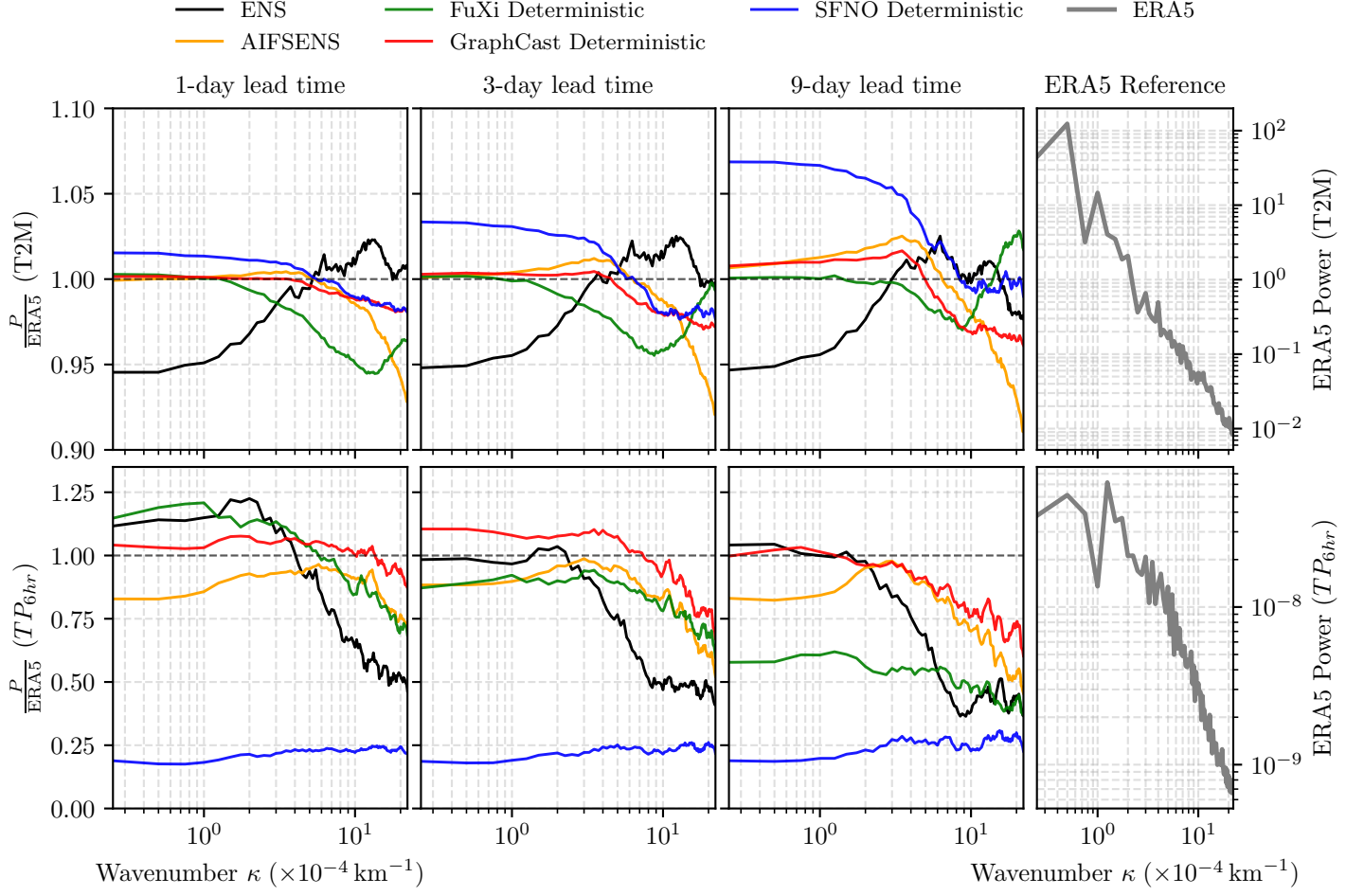


Figure 11: Spectral comparison of AIWP models against the ERA5 reanalysis for 2 m temperature (T2M, top row) and 6-hour accumulated precipitation ( $TP_{6hr}$ , bottom row). Each panel shows the smoothed power ratio,  $\frac{P}{P_{ERA5}}$ , as a function of wavenumber  $\kappa$  ( $\times 10^{-4} \text{ km}^{-1}$ ), for the ensemble mean of ENS and AIFSENS and the deterministic forecasts for FuXi, GraphCast, and SFNO, at forecast lead times of 1, 3, and 9 days. Values above 1 indicate excess variance relative to ERA5 (over-energetic spectra), while values under 1 indicate reduced small-scale variability (over-smoothing). The rightmost column displays the reference ERA5 power spectra for each variable.

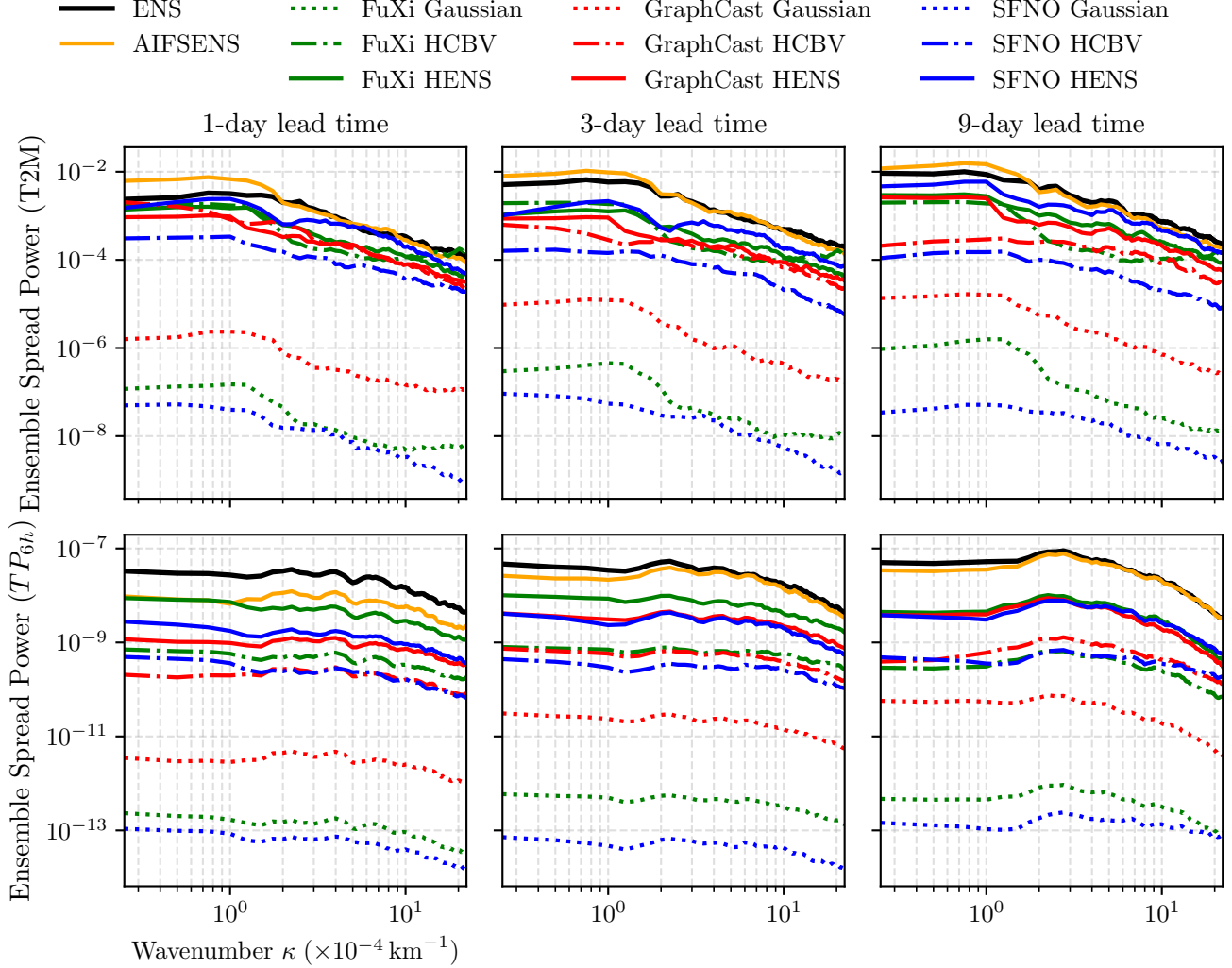


Figure 12: Ensemble spread spectral comparison for 2 m temperature (T2M, top row) and 6-hour accumulated precipitation ( $TP_{6hr}$ , bottom row). Each panel shows the smoothed ensemble spread spectral power, as a function of wavenumber  $\kappa$  ( $\times 10^{-4} \text{ km}^{-1}$ ), for ENS and AIFSENS, and the perturbed forecasts for FuXi, GraphCast, and SFNO, at forecast lead times of 1, 3, and 9 days, for a single initialization time in August 15th, 2022.

## References

- Gustau Camps-Valls, Miguel-Ángel Fernández-Torres, Kai-Hendrik Cohrs, Adrian Höhl, Andrea Castelletti, Aytac Pacal, Claire Robin, Francesco Martinuzzi, Ioannis Papoutsis, Ioannis Prapas, et al. Artificial intelligence for modeling and understanding extreme weather and climate events. *Nature Communications*, 16(1):1919, 2025.
- M Leutbecher and T N Palmer. Ensemble forecasting. *J. Comput. Phys.*, 227(7):3515–3539, March 2008. doi:<https://doi.org/10.1016/j.jcp.2007.02.014>.
- Kaifeng Bi, Lingxi Xie, Hengheng Zhang, Xin Chen, Xiaotao Gu, and Qi Tian. Accurate medium-range global weather forecasting with 3D neural networks. *Nature*, 619(7970):533–538, July 2023.
- Kang Chen, Tao Han, Junchao Gong, Lei Bai, Fenghua Ling, Jing-Jia Luo, Xi Chen, Leiming Ma, Tianning Zhang, Rui Su, Yuanzheng Ci, Bin Li, Xiaokang Yang, and Wanli Ouyang. Fengwu: Pushing the skillful global medium-range weather forecast beyond 10 days lead, 2023a. URL <https://arxiv.org/abs/2304.02948>.
- Lei Chen, Xiaohui Zhong, Feng Zhang, Yuan Cheng, Yinghui Xu, Yuan Qi, and Hao Li. FuXi: A cascade machine learning forecasting system for 15-day global weather forecast, October 2023b.
- Anna Allen, Stratis Markou, Will Tebbutt, James Requeima, Wessel P Bruinsma, Tom R Andersson, Michael Herzog, Nicholas D Lane, Matthew Chantry, J Scott Hosking, and Richard E Turner. End-to-end data-driven weather prediction. *Nature*, 641(8065):1172–1179, May 2025. doi:<https://doi.org/10.1038/s41586-025-08897-0>.
- Boris Bonev, Thorsten Kurth, Christian Hundt, Jaideep Pathak, Maximilian Baust, Karthik Kashinath, and Anima Anandkumar. Spherical Fourier Neural Operators: Learning Stable Dynamics on the Sphere, June 2023.
- Thorsten Kurth, Shashank Subramanian, Peter Harrington, Jaideep Pathak, Morteza Mardani, David Hall, Andrea Miele, Karthik Kashinath, and Anima Anandkumar. Fourcastnet: Accelerating global high-resolution weather forecasting using adaptive fourier neural operators. In *Proceedings of the Platform for Advanced Scientific Computing Conference, PASC '23*, New York, NY, USA, 2023. Association for Computing Machinery. ISBN 9798400701900. doi:10.1145/3592979.3593412. URL <https://doi.org/10.1145/3592979.3593412>.
- Ryan Keisler. Forecasting global weather with graph neural networks, 2022. URL <https://arxiv.org/abs/2202.07575>.
- Remi Lam, Alvaro Sanchez-Gonzalez, Matthew Willson, Peter Wirnsberger, Meire Fortunato, Ferran Alet, Suman Ravuri, Timo Ewalds, Zach Eaton-Rosen, Weihua Hu, Alexander Merose, Stephan Hoyer, George Holland, Oriol Vinyals, Jacklynn Stott, Alexander Pritzel, Shakir Mohamed, and Peter Battaglia. GraphCast: Learning skillful medium-range global weather forecasting. *Science*, December 2023. doi:10.1126/science.ad2336.
- Simon Lang, Mihai Alexe, Mariana C. A. Clare, Christopher Roberts, Rilwan Adewoyin, Zied Ben Bouallègue, Matthew Chantry, Jesper Dramsch, Peter D. Dueben, Sara Hahner, Pedro Maciel, Ana Prieto-Nemesio, Cathal O’Brien, Florian Pinault, Jan Polster, Baudouin Raoult, Steffen Tietsche, and Martin Leutbecher. AIFS-CRPS: Ensemble forecasting using a model trained with a loss function based on the Continuous Ranked Probability Score, December 2024a.
- Ilan Price, Alvaro Sanchez-Gonzalez, Ferran Alet, Tom R. Andersson, Andrew El-Kadi, Dominic Masters, Timo Ewalds, Jacklynn Stott, Shakir Mohamed, Peter Battaglia, Remi Lam, and Matthew Willson. GenCast: Diffusion-based ensemble forecasting for medium-range weather, May 2024.
- Lizao Li, Robert Carver, Ignacio Lopez-Gomez, Fei Sha, and John Anderson. Generative emulation of weather forecast ensembles with diffusion models. *Sci. Adv.*, 10(13):eadk4489, March 2024. doi:DOI:10.1126/sciadv.adk4489.
- Dmitrii Kochkov, Janni Yuval, Ian Langmore, et al. Neural general circulation models for weather and climate. *Nature*, 632:1060–1066, 2024. doi:10.1038/s41586-024-07744-y. URL <https://doi.org/10.1038/s41586-024-07744-y>.
- Noah D. Brenowitz, Yair Cohen, Jaideep Pathak, Ankur Mahesh, Boris Bonev, Thorsten Kurth, Dale R. Durran, Peter Harrington, and Michael S. Pritchard. A Practical Probabilistic Benchmark for AI Weather Models, November 2024.

- Jorge Baño-Medina, Agniv Sengupta, James D. Doyle, Carolyn A. Reynolds, Duncan Watson-Parris, and Luca Delle Monache. Are AI weather models learning atmospheric physics? A sensitivity analysis of cyclone Xynthia. *npj Climate and Atmospheric Science*, 8(1):1–9, March 2025a. ISSN 2397-3722. doi:10.1038/s41612-025-00949-6.
- Leonardo Olivetti and Gabriele Messori. Do data-driven models beat numerical models in forecasting weather extremes? A comparison of IFS HRES, Pangu-Weather, and GraphCast. *Geoscientific Model Development*, 17(21):7915–7962, November 2024. ISSN 1991-959X. doi:10.5194/gmd-17-7915-2024.
- Zhongwei Zhang, Erich Fischer, Jakob Zscheischler, and Sebastian Engelke. Numerical models outperform AI weather forecasts of record-breaking extremes, August 2025.
- Tongtiegang Zhao, Qiang Li, Tongbi Tu, and Xiaohong Chen. An extension of the WeatherBench 2 to binary hydroclimatic forecasts, February 2025.
- Stephan Rasp, Stephan Hoyer, Alexander Merose, Ian Langmore, Peter Battaglia, Tyler Russel, Alvaro Sanchez-Gonzalez, Vivian Yang, Rob Carver, Shreya Agrawal, Matthew Chantry, Zied Ben Bouallegue, Peter Dueben, Carla Bromberg, Jared Sisk, Luke Barrington, Aaron Bell, and Fei Sha. WeatherBench 2: A benchmark for the next generation of data-driven global weather models, January 2024.
- Franco Molteni, Roberto Buizza, Tim N Palmer, and Thomas Petrolia. The ecmwf ensemble prediction system: Methodology and validation. *Quarterly journal of the royal meteorological society*, 122(529):73–119, 1996.
- Sagar Garg, Stephan Rasp, and Nils Thuerey. WeatherBench Probability: A benchmark dataset for probabilistic medium-range weather forecasting along with deep learning baseline models, May 2022.
- M. Ponzano, B. Joly, I. Beau, E. Renard, and G. Fife. Bridging the gap between ensemble forecasting and end-user needs for decision-making on high-impact events. *Advances in Science and Research*, 22:39–52, 2025. doi:10.5194/asr-22-39-2025. URL <https://asr.copernicus.org/articles/22/39/2025/>.
- Christopher Bülte, Nina Horat, Julian Quinting, and Sebastian Lerch. Uncertainty quantification for data-driven weather models, March 2024.
- Ankur Mahesh, William Collins, Boris Bonev, Noah Brenowitz, Yair Cohen, Joshua Elms, Peter Harrington, Karthik Kashinath, Thorsten Kurth, Joshua North, Travis OBrien, Michael Pritchard, David Pruitt, Mark Risser, Shashank Subramanian, and Jared Willard. Huge Ensembles Part I: Design of Ensemble Weather Forecasts using Spherical Fourier Neural Operators, February 2025a.
- Xiaohui Zhong, Lei Chen, Hao Li, Roberto Buizza, Jun Liu, Jie Feng, Zijian Zhu, Xu Fan, Kan Dai, Jing-jia Luo, Jie Wu, and Bo Lu. FuXi-ENS: A machine learning model for efficient and accurate ensemble weather prediction. *Science Advances*, 11(44):eadu2854, October 2025. doi:10.1126/sciadv.adu2854.
- Ferran Alet, Ilan Price, Andrew El-Kadi, Dominic Masters, Stratis Markou, Tom R. Andersson, Jacklynn Stott, Remi Lam, Matthew Willson, Alvaro Sanchez-Gonzalez, and Peter Battaglia. Skillful joint probabilistic weather forecasting from marginals, June 2025.
- Guillaume Couairon, Renu Singh, Anastase Charantonis, Christian Lessig, and Claire Monteleoni. Archesweather and archesweathergen: a deterministic and generative model for efficient ml weather forecasting, 2024. URL <https://arxiv.org/abs/2412.12971>.
- Y. Qiang Sun, Pedram Hassanzadeh, Tiffany Shaw, and Hamid A. Pahlavan. Predicting Beyond Training Data via Extrapolation versus Translocation: AI Weather Models and Dubai’s Unprecedented 2024 Rainfall, May 2025.
- Bálint Mucsányi, Michael Kirchhof, and Seong Joon Oh. Benchmarking Uncertainty Disentanglement: Specialized Uncertainties for Specialized Tasks, November 2024.
- Katherine Haynes, Ryan Lagerquist, Marie McGraw, Kate Musgrave, and Imme Ebert-Uphoff. Creating and Evaluating Uncertainty Estimates with Neural Networks for Environmental-Science Applications. *Artificial Intelligence for the Earth Systems*, 2(2), April 2023. ISSN 2769-7525. doi:10.1175/AIES-D-22-0061.1.
- Eva-Maria Walz, Alexander Henzi, Johanna Ziegel, and Tilmann Gneiting. Easy Uncertainty Quantification (EasyUQ): Generating Predictive Distributions from Single-valued Model Output, July 2023.
- J. Baño-Medina, A. Sengupta, D. Watson-Parris, W. Hu, and L. Delle Monache. Toward Calibrated Ensembles of Neural Weather Model Forecasts. *Journal of Advances in Modeling Earth Systems*, 17(4):e2024MS004734, 2025b. ISSN 1942-2466. doi:10.1029/2024MS004734.

- Hans Hersbach, Bill Bell, Paul Berrisford, Shoji Hirahara, András Horányi, Joaquín Muñoz-Sabater, Julien Nicolas, Carole Peubey, Raluca Radu, Dinand Schepers, Adrian Simmons, Cornel Soci, Saleh Abdalla, Xavier Abellan, Gianpaolo Balsamo, Peter Bechtold, Gionata Biavati, Jean Bidlot, Massimo Bonavita, Giovanna De Chiara, Per Dahlgren, Dick Dee, Michail Diamantakis, Rossana Dragani, Johannes Flemming, Richard Forbes, Manuel Fuentes, Alan Geer, Leo Haimberger, Sean Healy, Robin J. Hogan, Elías Hólm, Marta Janisková, Sarah Keeley, Patrick Laloyaux, Philippe Lopez, Cristina Lupu, Gabor Radnoti, Patricia De Rosnay, Iryna Rozum, Freja Vamborg, Sebastien Villaume, and Jean-Noël Thépaut. The ERA5 global reanalysis. *Quarterly Journal of the Royal Meteorological Society*, 146(730):1999–2049, July 2020. ISSN 0035-9009, 1477-870X. doi:10.1002/qj.3803.
- Robert W. Carver and Alex Merose. ARCO-ERA5: An Analysis-Ready Cloud-Optimized Reanalysis Dataset. In *103rd AMS Annual Meeting*. AMS, January 2023.
- ECMWF. ECMWF IFS High-Resolution Operational Forecasts, 2016.
- Nicholas Geneva and Dallas Foster. NVIDIA Earth2Studio, April 2024.
- NVIDIA NGC Catalog. PhysicsNeMo Checkpoints: AFNO\_DX\_TP-V1-ERA5. [https://catalog.ngc.nvidia.com/orgs/nvidia/teams/earth-2/models/afno\\_dx\\_tp-v1-era5?version=v0.1.0](https://catalog.ngc.nvidia.com/orgs/nvidia/teams/earth-2/models/afno_dx_tp-v1-era5?version=v0.1.0), April 2025.
- Simon Lang, Mihai Alexe, Matthew Chantry, Jesper Dramsch, Florian Pinault, Baudouin Raoult, Mariana C. A. Clare, Christian Lessig, Michael Maier-Gerber, Linus Magnusson, Zied Ben Bouallègue, Ana Prieto Nemesio, Peter D. Dueben, Andrew Brown, Florian Pappenberger, and Florence Rabier. AIFS – ECMWF’s data-driven forecasting system, August 2024b.
- Jie Feng, Jianping Li, Ruiqiang Ding, and Zoltan Toth. Comparison of Nonlinear Local Lyapunov Vectors and Bred Vectors in Estimating the Spatial Distribution of Error Growth. *Journal of the Atmospheric Sciences*, 75(4):1073–1087, April 2018. ISSN 0022-4928, 1520-0469. doi:10.1175/JAS-D-17-0266.1.
- Zoltan Toth and Eugenia Kalnay. Ensemble Forecasting at NCEP and the Breeding Method. *Monthly Weather Review*, 125(12):3297–3319, December 1997. ISSN 1520-0493, 0027-0644. doi:10.1175/1520-0493(1997)125<3297:EFANAT>2.0.CO;2.
- Zoltan Toth and Eugenia Kalnay. Ensemble forecasting at NMC: The generation of perturbations. *Bull. Am. Meteorol. Soc.*, 74(12):2317–2330, December 1993. doi:https://doi.org/10.1175/1520-0477(1993)074<2317:EFANTG>2.0.CO;2.
- Bohar Singh, Muhammad Azhar Ehsan, and Andrew W Robertson. Calibrated probabilistic sub-seasonal forecasting for pakistan’s monsoon rainfall in 2022. *Clim. Dyn.*, 62(5):3375–3393, May 2024.
- Zhiying Sun, Chen Chen, Meilin Yan, Wanying Shi, Jiaonan Wang, Jie Ban, Qinghua Sun, Mike Z He, and Tiantian Li. Heat wave characteristics, mortality and effect modification by temperature zones: A time-series study in 130 counties of China. *International Journal of Epidemiology*, 49(6):1813–1822, January 2021. ISSN 0300-5771, 1464-3685. doi:10.1093/ije/dyaa104.
- Arfan Arshad, Ali Mirchi, Cenlin He, Azeem Ali Shah, and Amir AghaKouchak. Anthropogenic and climatic drivers of the 2022 mega-flood in pakistan. *NPJ Nat. Hazards*, 2(1), July 2025. doi:https://doi.org/10.1038/s44304-025-00109-z.
- Chi-Cherng Hong, An-Yi Huang, Huang-Hsiung Hsu, Wan-Ling Tseng, Mong-Ming Lu, and Chih-Chun Chang. Causes of 2022 Pakistan flooding and its linkage with China and Europe heatwaves. *npj Climate and Atmospheric Science*, 6(1):1–10, October 2023. ISSN 2397-3722. doi:10.1038/s41612-023-00492-2.
- Khurram Shehzad. Extreme flood in pakistan: Is pakistan paying the cost of climate change? a short communication. *Sci. Total Environ.*, 880(162973):162973, July 2023. doi:https://doi.org/10.1016/j.scitotenv.2023.162973.
- Farah Ikram, Muhammad Karori, Ahsan Syed, and Burhan Ahmad. Past and future trends in frequency of heavy rainfall events over Pakistan. *Pakistan Journal of Meteorology*, 12:57–78, February 2016.
- Hainan Gong, Kangjie Ma, Zhiyuan Hu, Zizhen Dong, Yuanyuan Ma, Wen Chen, Renguang Wu, and Lin Wang. Attribution of the August 2022 Extreme Heatwave in Southern China: Role of Dynamical and Thermodynamical Processes. *Bulletin of the American Meteorological Society*, 105(1):E193–E199, January 2024. ISSN 0003-0007, 1520-0477. doi:10.1175/BAMS-D-23-0175.1.
- Bingqian Zhou, Shujuan Hu, Jianjun Peng, Deqian Li, Lu Ma, Zhihai Zheng, and Guolin Feng. The extreme heat wave in China in August 2022 related to extreme northward movement of the eastern center of SAH. *Atmospheric Research*, 293:106918, September 2023. ISSN 0169-8095. doi:10.1016/j.atmosres.2023.106918.

- Bo Sun, Huijun Wang, Yanyan Huang, Zhicong Yin, Botao Zhou, and Mingkeng Duan. Characteristics and causes of the hot-dry climate anomalies in China during summer of 2022. *Trans Atmos Sci*, 46(1):1–8, March 2023. doi:10.13878/j.cnki.dqkxxb.20220916003.
- Ankur Mahesh, William Collins, Boris Bonev, Noah Brenowitz, Yair Cohen, Peter Harrington, Karthik Kashinath, Thorsten Kurth, Joshua North, Travis OBrien, Michael Pritchard, David Pruitt, Mark Risser, Shashank Subramanian, and Jared Willard. Huge Ensembles Part II: Properties of a Huge Ensemble of Hindcasts Generated with Spherical Fourier Neural Operators, February 2025b.
- Mark J. Rodwell, Mariana C. A. Clare, Sarah-Jane Lock, Katrin Lonitz, and Matthieu Chevallier. Power Spectra of Physics-Based and Data-Driven Ensembles. *Meteorological Applications*, 32(5):e70071, 2025. ISSN 1469-8080. doi:10.1002/met.70071.
- David A. Lavers, Adrian Simmons, Freja Vamborg, and Mark J. Rodwell. An evaluation of ERA5 precipitation for climate monitoring. *Quarterly Journal of the Royal Meteorological Society*, 148(748):3152–3165, 2022. ISSN 1477-870X. doi:10.1002/qj.4351.
- Aman Gupta, Aditi Sheshadri, and Dhruv Suri. MAUSAM: An Observations-focused assessment of Global AI Weather Prediction Models During the South Asian Monsoon, September 2025.
- Ye Yang, Meng Gao, Naru Xie, and Zhiqiang Gao. Relating anomalous large-scale atmospheric circulation patterns to temperature and precipitation anomalies in the East Asian monsoon region. *Atmospheric Research*, 232:104679, February 2020. ISSN 0169-8095. doi:10.1016/j.atmosres.2019.104679.
- Philipp Hess and Niklas Boers. Deep Learning for Improving Numerical Weather Prediction of Heavy Rainfall. *Journal of Advances in Modeling Earth Systems*, 14(3):e2021MS002765, March 2022. ISSN 1942-2466, 1942-2466. doi:10.1029/2021MS002765.
- W Weibull. Astatistical theory ofthe strength of materials. *Proc. Royal Academy Engrg Science*, 15(1):1, 1939.